

Tunable-Generalization Diffusion Powered by Self-Supervised Contextual Sub-Data for Low-Dose CT Reconstruction

Guoquan Wei, Liu Shi, Zekun Zhou, Wenzhe Shan, Qiegen Liu, *Senior Member, IEEE*

Abstract—Current models based on deep learning for low-dose CT denoising rely heavily on paired data and generalize poorly. Even the more concerned diffusion models need to learn the distribution of clean data for reconstruction, which is difficult to satisfy in medical clinical applications. At the same time, self-supervised-based methods face the challenge of significant degradation of generalizability of models pre-trained for the current dose to expand to other doses. To address these issues, this work proposes a novel method of Tunable-generalization Diffusion (TurnDiff) powered by self-supervised contextual sub-data for low-dose CT reconstruction. Firstly, a contextual subdata self-enhancing similarity strategy is designed for denoising centered on the LDCT projection domain, which provides an initial prior for the subsequent progress. Subsequently, the initial prior is used to combine knowledge distillation with a deep combination of latent diffusion models for optimizing image details. The pre-trained model is used for inference reconstruction, and the pixel-level self-correcting fusion technique is proposed for fine-grained reconstruction of the image domain to enhance the image fidelity, using the initial prior and the LDCT image as a guide. In addition, the technique is flexibly applied to the generalization of upper and lower doses or even unseen doses. Dual-domain strategy cascade for self-supervised LDCT denoising, TurnDiff requires only LDCT projection domain data for training and testing. Comprehensive evaluation on both benchmark datasets and real-world data demonstrates that TurnDiff consistently outperforms state-of-the-art methods in both reconstruction and generalization.

Index Terms—Low-dose CT reconstruction, self-supervised, diffusion model, tunable generalization.

I. INTRODUCTION

COMPUTED tomography (CT) is a clinically established imaging technique whose inherent radiation exposure may increase cancer risk [1], [2]. Low-dose CT (LDCT) reduces radiation dose by decreasing tube current, yet introduces severe noise and artifacts that degrade diagnostic quality [3].

This work was supported by the National Natural Science Foundation of China (621220033, 62201193). (G. Wei is the first author.) (Co-corresponding authors: L. Shi and Q. Liu.)

G. Wei, L. Shi, W. Shan, and Q. Liu are with School of Information Engineering, Nanchang University, Nanchang 330031, China (email: {shiliu, shan, liuqiegen}@ncu.edu.cn, guoquanwei@email.ncu.edu.cn).

Z. Zhou is with School of Mathematics and Computer Sciences, Nanchang University, Nanchang 330031, China (email: zekunzhou@email.ncu.edu.cn).

Over the past few decades, LDCT reconstruction has produced numerous commendable results. These studies fall into three main categories: 1) sinusoidal domain data filtering [4], 2) iterative reconstruction [5], and 3) image post-processing techniques [6]. Sinusoidal domain filtering, such as bilateral filtering method [7], penalized weighted least squares (PWLS) [8], etc., operates directly on projection data but risk losing frequency information and reducing spatial resolution. Iterative reconstruction is often limited in clinical application due to its high computational cost and complexity. Image post-processing techniques are applied to the reconstructed LDCT images to enhance the image quality, such as block matching based 3D filtering (BM3D) [9] demonstrates excellent performance in LDCT imaging.

In recent years, deep learning (DL) has surpassed traditional methods in medical imaging applications like CT reconstruction, where data-driven models are trained to denoise images [10], [11]. However, current deep learning based methods either use supervised methods that rely on paired data [12], [13] or self-supervised methods with paired noise [14], self-supervised learning with batch data similarity [15] or unsupervised learning with clean data using diffusion models [16]. The dominant supervised approach is clinically hampered. Acquiring the necessary real, paired low- and normal-dose data from a single patient is infeasible. This makes self-supervised learning, which trains solely on noisy images, a more practical clinical solution. However, current self-supervised methods still need to address the problem of poor reconstruction of untrained doses.

Diffusion modeling (DM) [17] has recently emerged as a novel and influential explicit generative model that has been widely used in medical image reconstruction with impressive results. Although DM has been shown to achieve high-quality reconstruction [18], the standard diffusion model still suffers from 1) long sampling time of 1000 steps, difficult to train with high resolution, and difficulty in lightweight deployment [19]. 2) In the absence of real data distribution involved, the results are usually not good. For this reason, a series of methods such as accelerated samplers [20], domain iterative diffusion [21], latent diffusion [22], and guided diffusion [23] have emerged.

In order to fit the clinical application, the aim of this work is to explore a low-dose denoising method that relies only on a single noise projection domain and does not rely on the distribution of clean data for modeling. To this end, this study proposes tunable-generalization diffusion for low-dose

CT reconstruction. A contextual LDCT projection domain self-enhancing similarity strategy is designed to adequately remove the noise under the data domain. The results are further optimized in the image domain considering the complexity of noise and incomplete detail recovery. For this purpose, the initial prior is used to deeply combine the knowledge distillation technique with the latent diffusion model to perceive the data consistency and refinement. In the inference stage, the initial prior and LDCT images are introduced as a guide to fully utilize the model effectiveness as well as the matching training process. On this basis, a pixel-level self-correcting fusion is proposed to balance the differences between the bootstrap information, and the technique is skillfully applied to the generalization of the upper and lower doses as well as the dose of unseen data.

In summary, the work of this paper can be described as:

- A novel self-supervised denoising model TurnDiff starting from a single sheet of noisy projection data is proposed. A self-enhancing similarity strategy for contextual projection sub-data is designed for sufficiently removing the nonlinear noise under the projection domain to provide an effective initial prior.
- Knowledge distillation is deeply combined with latent diffusion model. Mapping the image domain to the latent space, with the help of Gaussian diffusion mechanism and transformer denoising network to fully perceive the details and enhance the reconstruction effect.
- TurnDiff exploits the projection domain prior and the LDCT image as a guide in the inference phase, and the pixel-level self-correcting fusion technique improves the balance between the two, facilitating data fidelity and lesion reproduction. The technique is also used for tunable generalization of up and down dose, unseen dose and real clinical data.

II. RELATED WORK

This section begins with statistical theory-based denoising methods, progresses to approaches leveraging CT data features, and concludes with recent advances in diffusion models for denoising and reconstruction.

A. Denoising Research under Statistical Theory

Given a LDCT projection measure y_{ld} , the inverse problem is to recover to clean data y_0 . The corresponding image domain is as follows:

$$y_{ld} \approx Ax_0 + \epsilon_y, x_{ld} = \mathcal{R}(y_{ld}) = \underbrace{x_0 + bias}_{\mathcal{R}(Ax_0)} + \underbrace{\epsilon_x}_{\mathcal{R}(\epsilon_y)}, \quad (1)$$

where A is the projection matrix, ϵ_y is the projection noise, \mathcal{R} is the back-projection operator, and ϵ_x is the reconstruction noise term.

Noise2Noise [14] eliminated the need for clean data or paired training samples by utilizing pairs of independent noisy realizations x_{ld} and x'_{ld} , thereby achieving an effect equivalent to supervised learning with clean reference x_0 during training.

The statement is as follows:

$$\begin{aligned} & \min_{\theta} \{ \mathbb{E} \| f_{\theta}(x'_{ld}) - x_{ld} \|^2 \} \\ & \approx \min_{\theta} \{ \mathbb{E} \| f_{\theta}(x'_{ld}) - x_0 \|^2 + \mathbb{E} \| x_{ld} - x_0 \|^2 \} \end{aligned} \quad (2)$$

where $f_{\theta}(\cdot)$ represents a neural network driven by θ . However, this method requires two independent noise measurements of the same information and is not strictly self-supervised.

On this basis, Noise2Self [24] extended J-invariance theory by focusing on the input x_{ld} . Noiser2Noise [25] constructed training pairs by adding further noise to noisy images. Neighbor2Neighbor [26] offered an efficient self-supervision approach using adjacent subsamples from a single noisy image. These methods generally suffered from poor performance in CT imaging, where reconstruction steps like log transformation, interpolation, and filtering altered noise distribution and introduced spatial correlation.

Consequently, CT-specific noise optimization has been explored. Niu *et al.* [15] used patient-specific similar data as denoising targets, though random selection limited generalization. Wang *et al.* [27] improved the selection strategy and introduced a visual blind-spot technique. These batch-based methods require aligned Z-axis CT data. Other studies leverage CT imaging principles: Wu *et al.* [28] applied guided filtering to unsharp CT image structures, while Proj2Proj [29] demonstrated self-supervised denoising directly in projection space, validating denoising starting from the projection domain.

B. Diffusion Models

The diffusion model, as a generative model obeying a Markov chain, is designed to learn an approximate distribution of the data in the forward noise addition and inverse denoising process. The forward process is constructed by adding noise to the given target data:

$$q(x_t|x_0) = \mathcal{N}(x_t; \sqrt{\bar{\alpha}_t}x_0, (1 - \bar{\alpha}_t)\mathbf{I}), \quad (3)$$

$$x_t = \sqrt{\bar{\alpha}_t}x_0 + \sqrt{1 - \bar{\alpha}_t}\epsilon, \epsilon \sim \mathcal{N}(0, \mathbf{I}), \quad (4)$$

where $\bar{\alpha}_t$ is a hyperparameter that controls the noise level, and the forward process adds noise up to $x_T \sim \mathcal{N}(0, \mathbf{I})$. The backward process then progressively predicts from x_T until it approaches x_0 .

$$p_{\theta}(x_{t-1}|x_t) = \mathcal{N}(x_{t-1}; \boldsymbol{\mu}_{\theta}(x_t, t), \sigma_t^2 \mathbf{I}), \quad (5)$$

$$\boldsymbol{\mu}_{\theta}(x_t, t) = \frac{1}{\sqrt{\alpha_t}} \left(x_t - \frac{1 - \alpha_t}{\sqrt{1 - \bar{\alpha}_t}} \epsilon_{\theta}(x_t, t) \right), \sigma_t^2 = 1 - \alpha_t, \quad (6)$$

where ϵ_{θ} is a noise predictor driven by a neural network.

Recent extensions of diffusion models include the score-based generative model by Song *et al.* [18], which utilized stochastic differential equations (SDEs). Gao *et al.* [30] developed CoreDiff, a cold diffusion-based model preserving physical degradation properties, later extended to the dual-domain model NEED [31], which incorporates offset Poisson diffusion in the projection domain and dual-guided diffusion in the image domain for improved reconstruction. Liao *et al.* [21] designed a dual-domain denoising model that enhances sampling efficiency through an iterative partial diffusion process.

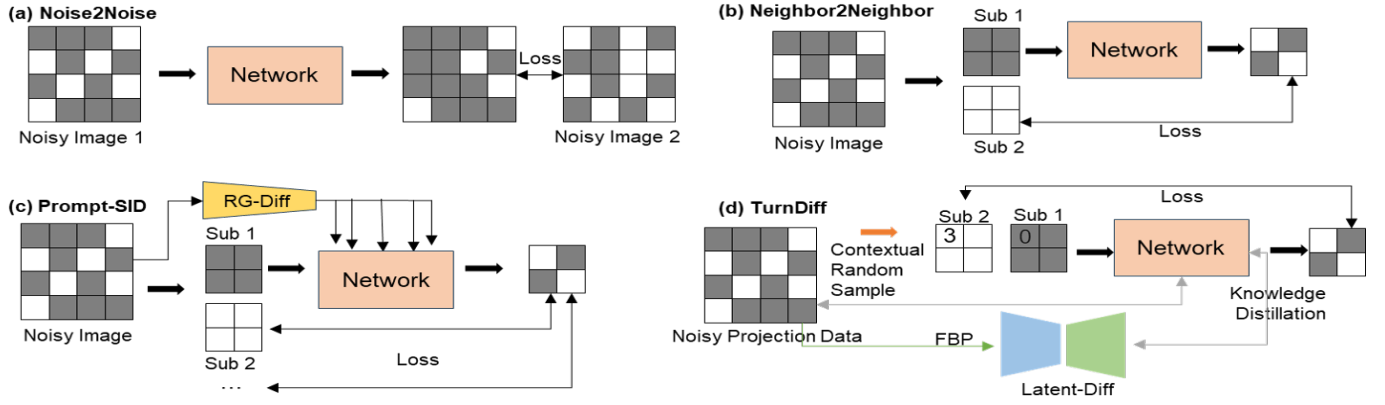


Fig. 1. Visual demonstration of the differences among (a) Noise2Noise, (b) Neighbor2Neighbor, (c) Prompt-SID and (d) TurnDiff.

Yang *et al.* [32] proposed a latent feature-guided diffusion model applicable to multimodal image fusion tasks. Li *et al.* [33] proposed Prompt-SID, which introduces structural cue learning and a scale replay mechanism in latent space to bridge resolution gaps for self-supervised denoising. Fig. 1 provides an overview of the progress in self-supervised denoising research.

III. METHOD

This section presents a projection-domain denoising model using contextual sub-data, followed by an image-domain latent distillation stage. It further details a pixel-wise self-correcting fusion mechanism and tunable generalization strategy, with the overall framework illustrated in Fig. 2.

A. Projection Domain Contextual Sub-data Denoising

At present, the noise generated in the LDCT scanning process mainly comes from the quantum noise caused by photon fluctuation and the electronic noise caused by the equipment itself. And the image domain data under the filtered backprojection is prone to bring stronger spatial correlation. According to Eq. (2), following the noise-to-noise principle can realize that targeting noise is equivalent to recovering to a clean image. To this end, this study proposes a randomized contextual subdata sampling strategy $s(\cdot)$. Firstly, the noise-containing projection y_{ld} is divided into $H_y/2 \times W_y/2$ chunks, each chunk contains four data points, and one point is randomly selected among the four data points i , the remaining three are the lower data point $i-1$ or the upper data point $i+1$, $i+2$ of that point, when $i=0$ or $i=3$ there is only the upper data point or the lower data point. As shown in Fig. 3, the selected data points are divided into different sampling data. The random selection strategy can be described as:

$$(s_i(y_{ld}), s_j(y_{ld})) \sim \mathcal{U}\{s_1(y_{ld}), s_2(y_{ld}), s_3(y_{ld})\}, \quad i \neq j, \quad (7)$$

where $(s_i(\cdot), s_j(\cdot)) \sim \mathcal{U}(\cdot)$ represents the sub-data of context features after uniform sampling.

According to lemma 1 of [14], and the proof of [34]. Assuming that noisy image pairs a and b are conditionally independent given a clean image x_0 , and that the gap between

the two is defined as $\varepsilon := \mathbb{E}_{b|x_0}(b) - \mathbb{E}_{a|x_0}(a)$, the relationship between the noisy data pairs and the supervised training loss is defined as:

$$\mathbb{E}_{x_0, a} \|f_\theta(a) - x_0\|_2^2 = \mathbb{E}_{x_0, a, b} \|f_\theta(a) - b\|_2^2 - \sigma_b^2 + 2\varepsilon \mathbb{E}_{x_0, a}(f_\theta(a) - x_0), \quad (8)$$

where σ_b^2 is the variance of b , when $\varepsilon \rightarrow 0$, optimizing $\mathbb{E}_{x_0, a, b} \|f_\theta(a) - b\|_2^2$ is equivalent to optimizing the supervised loss. Similarly, $s_1(y_{ld})$ and $s_2(y_{ld})$ are context pixels in y_{ld} , and there is always a certain similarity.

To enhance similarity in the data, this study introduces a self-enhancing similarity strategy that dynamically excludes regions with significant disparities between contextual sub-data. The term pairs $(s_1(y_{ld}), s_2(y_{ld}))$ and $(s_1(f_\theta(y_{ld})), s_2(f_\theta(y_{ld})))$ are defined to satisfy $\varepsilon_1 = \mathbb{E}_{y_{ld}|y_0}(s_1(y_{ld})) - \mathbb{E}_{y_{ld}|y_0}(s_2(y_{ld}))$ and $\varepsilon_2 = \mathbb{E}_{y_{ld}|y_0}(s_1(f_\theta(y_{ld}))) - \mathbb{E}_{y_{ld}|y_0}(s_2(f_\theta(y_{ld})))$. After extracting differential regions, the model dynamically propagates this result to the supervision loss calculation. The objective function can be defined as:

$$\begin{aligned} \min_{\theta} \mathbb{E}_{y_0, y_{ld}} \| & (f_\theta(s_1(y_{ld})) - s_2(y_{ld})) \odot (1 - \varepsilon_1) \|_2^2 \\ & + \alpha \mathbb{E}_{y_0, y_{ld}} \| (f_\theta(s_1(y_{ld})) - s_2(y_{ld})) \odot (1 - \varepsilon_1) \\ & - (s_1(f_\theta(y_{ld})) - s_2(f_\theta(y_{ld}))) \odot (1 - \varepsilon_2) \|_2^2, \end{aligned} \quad (9)$$

where \odot represents element-by-element multiplication and α is empirically set to 0.02. For detailed information about Eq. (9), please refer to the Appendix.A.

The initial denoised projection data \hat{y}_0 can be obtained after the above processing. The initial reconstructed image domain \hat{x}_0 can be described as:

$$\hat{x}_0 = \text{FBP}(\hat{y}_0). \quad (10)$$

B. Latent Diffusion Image Refinement

While projection-domain denoising significantly reduces noise, the initial reconstruction \hat{x}_0 often exhibits residual blurring and incomplete noise removal. Further same processing may introduce error accumulation due to strong spatial correlations in CT images, leading to deviated optimization trajectories and information degradation. To address this, we introduce a latent diffusion model (LDM)-based denoising

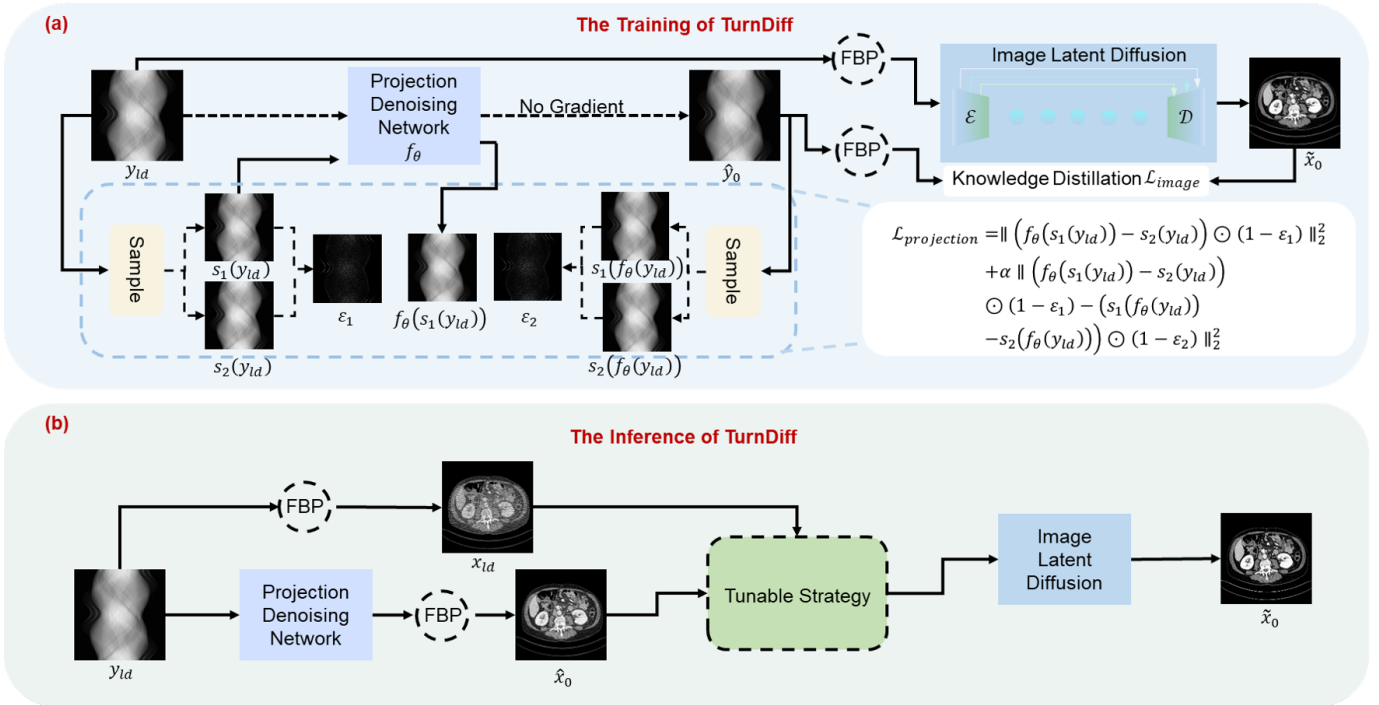


Fig. 2. General Architecture of TurnDiff Training and Inference. (a) The training of TurnDiff. (b) The inference of TurnDiff.

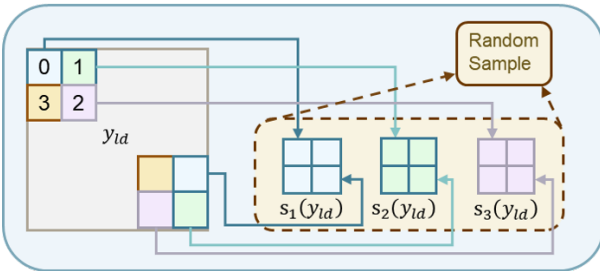


Fig. 3. Description of random sampling of contextual projection data.

framework that leverages Gaussian diffusion in latent space to learn uncorrupted features for refined image enhancement.

Conventional LDMs require clean-image pretraining for task-specific encoders, which contradicts self-supervised denoising from a single projection. To resolve this, we adopt the U-Net-based encoder-decoder structure from Yang *et al.* [32], which effectively maps images into a lower-dimensional latent space while preserving high-frequency noise patterns. Based on formulas Eqs. (3)–(5), the diffusion model is defined as follows:

$$x_{ld}^L = \mathcal{E}(x_{ld}), \quad (11)$$

$$\tilde{x}_0 = D(x_0^L), \quad (12)$$

where \mathcal{E} represents the pixel-level encoder used to map x_{ld} to the latent space variable x_{ld}^L . x_0^L represents the latent space variable to be decoded after denoising. D is then the decoded compression variable x_0^L for the final denoised CT image \tilde{x}_0 .

To leverage the intermediate representation of the initial reconstruction \hat{x}_0 , this study integrates knowledge distillation into the LDM framework. 1) The pre-trained projection-domain model yields \hat{x}_0 as a representation-constrained prior.

2) x_{ld} is compressed into a low-dimensional latent space via Eq. (11), then progressively degraded to Gaussian noise x_T via Eq. (3). 3) A transformer-based noise prediction network $\epsilon_\theta(\cdot)$ is trained with Eq. (5) to focus on low-frequency information for inverse denoising, generating x_0^L , which is subsequently decoded via Eq. (12). 4) Iterative training, using \hat{x}_0 as a constrained prior, distills \tilde{x}_0 , which has more complete feature information. The reverse process uses only 5 sampling steps, ensuring high efficiency. Therefore, the loss in this stage contains diffusion loss and denoising loss:

$$\mathcal{L}_{\text{image}} = \mathcal{L}_{\text{diff}} + \mathcal{L}_{\text{denoising}}, \quad (13)$$

where $\mathcal{L}_{\text{diff}}$ represents minimizing the difference between the denoising network prediction noise $\epsilon_\theta(x_t, t)$ and the initial sampling noise ϵ .

The denoising loss is designed to exploit knowledge distillation for better fine-grained generation. The definition is as follows:

$$\begin{aligned} \mathcal{L}_{\text{denoising}} &= \beta \mathcal{L}_{\text{ssim}} + \gamma \mathcal{L}_{\text{grad}} + \eta \mathcal{L}_{11} \\ &= \beta (1 - \text{ssim}(\mathcal{D}(x_t^L), x_0)) + \gamma \frac{1}{H_x W_x} \|\ |\nabla \hat{x}_0| - |\nabla \mathcal{D}(x_t^L)| \|_1 \\ &\quad + \eta \frac{1}{H_x W_x} \|\ \hat{x}_0 - \mathcal{D}(x_t^L) \|_1, \end{aligned} \quad (14)$$

where β , γ , η represent the weights of each loss, which are empirically set to 1.0, 2.0, 0.5. ∇ represents the Sobel-based gradient operator. x_t^L represents a certain latent state that is not fully denoised.

C. Tunable Generalization for Up- and Down-dose

1) *Pixel-level self-correcting fusion reconstruction*: A trained projection domain model and an image domain model using

a single projection domain are used for LDCT dual-domain reconstruction. When the dual-domain model cascade is performed for reconstruction, if the initial reconstruction \hat{x}_0 in the projection domain is used as the starting point of the image domain stage, it may have the effect of over-suppressing the noise and destroying the medical lesions. To address this, we introduce a weighted fusion of the original LDCT image x_{ld} and the initial reconstruction \hat{x}_0 to guide the image-domain reconstruction. This approach compensates for information lost in the projection domain while avoiding the introduction of excessive noise and artifacts. Unlike previous methods that rely on fixed weights or scalar adaptive weights, our method accounts for the non-uniform spatial distribution of noise and anatomical features through pixel-level adaptive weighting.

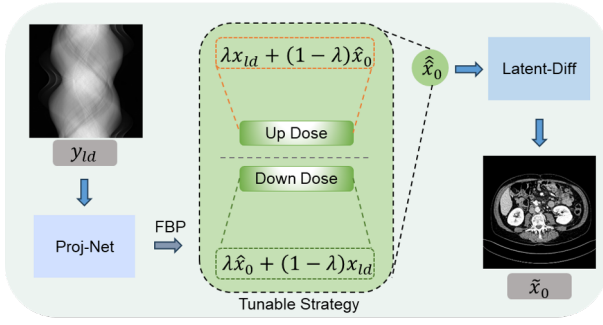


Fig. 4. Tunable up- and down-dose generalization strategy.

Specifically, the fusion process is guided by two confidence measures: an edge confidence map C_e derived from \hat{x}_0 and a noise confidence map C_n estimated from x_{ld} . The description is as follows:

$$C_e = \sigma(k_2(G_{\hat{x}_0} - \tau_e)), C_n = \sigma(k_1(N_{x_{ld}} - \tau_n)), \quad (15)$$

$$\lambda = \mathcal{F}(C_e, C_n, N_{x_{ld}}^{25\%}), \quad (16)$$

where C_e and C_n are the edge confidence and noise confidence. $\sigma(z) = \frac{1}{1+e^{-z}}$ and $\tau_e = \text{sort}(G_{\hat{x}_0}, 0.8)$, $\tau_n = \text{sort}(N_{x_{ld}}, 0.8)$. $G_{\hat{x}_0}$ is the gradient magnitude and $N_{x_{ld}}$ is the noise level estimate. $\lambda \in \mathbb{R}^{B_x \times C_x \times H_x \times W_x}$ exists as pixel-level weights. So the image into the image domain is represented as:

$$\hat{x}_0 = \underbrace{\lambda x_{ld}}_{\text{LDCT term}} + \underbrace{(1-\lambda)\hat{x}_0}_{\text{middle term}}, \quad (17)$$

where λ must not be all 1, otherwise this is contrary to the original purpose of cascading dual-domain denoising, \hat{x}_0 is the image to be denoised into the image domain pre-training model, and then denoised by the Eq. (14) pre-trained model to get our final reconstructed image \tilde{x}_0 .

2) Tunable strategies of up and down dose generalization:

Define $\mathcal{F}(\cdot)$ as the key function for tunable generalization, with $N_{x_{ld}}^{25\%}$ representing the noise level at 25% dose. Currently, the dose distribution of LDCT is generally between 5% and 50% dose, with 25% as the boundary, 5% – 25% is the down dose, and 25% – 50% is the up dose. The definition is as follows:

$$\mathcal{F}(C_e, C_n, N_{x_{ld}}^{25\%}) = \begin{cases} \lambda_{up} & S \leq S_0 \\ \lambda_{down} & S > S_0 \end{cases}, \quad (18)$$

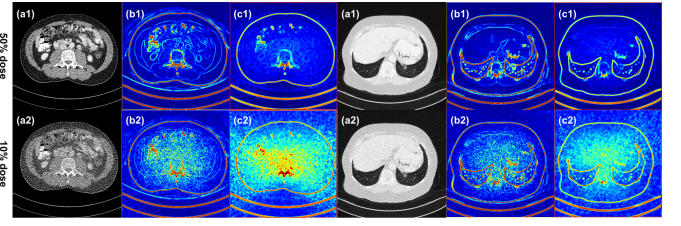


Fig. 5. $\{(a1), (a2)\}$: noisy images, $\{(b1), (b2)\}$: the edges extracted from \hat{x}_0 , and $\{(c1), (c2)\}$: the noise level estimated from x_{ld} .

where $S = \text{sum}(N_{x_{ld}})$, $S_0 = \text{sum}(N_{x_{ld}}^{25\%})$, $\lambda_{up} = \text{Clip}(C_n + C_e, 0, 1)$, $\lambda_{down} = 1 - \text{Clip}(C_n + C_e, 0, 1)$, $\text{sum}(\cdot)$ denotes pixel-wise noise level summation. Different noise levels determine whether λ tends to favor x_{ld} or \hat{x}_0 . Detailed description is shown in Fig. 4 and Fig. 5.

Algorithm 1 Training and Inference Process

Input: Single LDCT projection data y_{ld} , designed $s(\cdot)$, total time steps T and sampling steps T_L

Output: Well-trained models f_θ , \mathcal{E} , \mathcal{D} and ϵ_θ ; Reconstructed image \tilde{x}_0

1: Training Phase:

2: Repeat:

3: Calculate $s_1(y_{ld})$, $s_2(y_{ld})$ by Eq. (7)

4: Update f_θ by Eq. (9)

5: Update \mathcal{E} , \mathcal{D} , ϵ_θ by Eq. (13)

6: Until converged

7: Inference Phase:

8: $\hat{y}_0 \leftarrow f_\theta(y_{ld})$

9: Calculate \hat{x}_0 by Eq. (10)

10: Calculate $\hat{\hat{x}}_0$ by Eq. (17)

11: $\hat{\hat{x}}_0^L \leftarrow \mathcal{E}(\hat{\hat{x}}_0)$

12: **for** $t = T, T - (T/T_L), \dots, 1$ **do**

13: Calculate $\hat{\hat{x}}_{t-1}^L$ by Eq. (5)

14: **end for**

15: Calculate \tilde{x}_0 by Eq. (12)

IV. EXPERIMENTS

This section focuses on the dataset used in this study, the simulation approach, the experimental details, and the evaluation metrics. Subsequently, the proposed method is thoroughly evaluated by quantitatively and qualitatively comparing it with the current state-of-the-art denoising methods. Next, the method is applied to a real clinical scenario for validation. Finally, ablation studies are designed to verify the validity of this study.

A. Datasets

1) *Mayo dataset*: The Mayo dataset [35] from AAPM Grand Challenge was used to validate the algorithms, which consisted of the NDCT data and the corresponding simulated LDCT data from 10 patients. In this study, in order to obtain data at different doses, a simulated LDCT method similar to the study of [36] was used. It can be described as:

$$y_{ld} = \ln \frac{I_0}{\text{Poisson}(I_0 \exp(-y_0)) + \text{Gaussian}(0, \sigma_e^2)}, \quad (19)$$

TABLE I

QUANTITATIVE RESULTS (MEAN±STD) ON 25% DOSE LEVEL FROM THE MAYO 2016 DATASET AND THE LIDC-IDRI DATASET. THE BEST RESULTS ARE HIGHLIGHTED IN BOLD.

Methods	Mayo Dataset						LIDC-IDRI Dataset					
	PSNR ↑	SSIM(%) ↑	RMSE ↓	FSIM(%) ↑	VIF(%) ↑	NQM ↑	PSNR ↑	SSIM(%) ↑	RMSE ↓	FSIM(%) ↑	VIF(%) ↑	NQM ↑
Baseline/Tradition												
FBP	31.89±2.58	70.00±10.27	53.17±15.93	94.74±2.73	24.60±7.51	28.06±2.89	36.39±3.43	84.28±9.91	32.73±14.90	96.84±2.30	37.10±13.74	31.35±2.69
TV	38.21±2.47	94.30±2.49	24.74±9.21	95.31±1.31	61.21±13.52	22.03±2.68	40.05±1.31	96.03±0.82	20.03±3.61	94.68±3.10	62.10±9.80	28.14±1.51
Self-supervised												
B2U	32.83±2.39	73.41±9.69	47.44±13.66	96.02±2.04	26.29±8.17	26.86±2.55	36.78±3.61	85.22±9.80	31.58±13.07	97.10±2.17	39.29±14.94	30.02±2.59
Neighbor2Neighbor	39.02±2.35	92.41±3.92	23.25±6.79	98.22±0.81	53.37±11.39	27.47±2.58	41.59±2.40	96.01±2.61	17.32±5.28	98.68±0.63	64.41±13.60	30.65±2.38
Noiser2Noise	38.22±2.53	92.52±5.24	25.78±9.42	97.05±0.63	61.58±12.84	24.28±1.15	38.34±0.95	96.15±0.97	24.33±2.69	96.91±0.69	67.62±4.61	21.39±0.79
Prompt-SID	36.71±2.51	87.21±6.03	30.47±9.20	98.05±0.99	41.72±10.78	28.18±2.58	40.43±2.77	94.05±3.97	20.04±6.78	98.86±0.70	56.37±14.73	31.42±2.32
Noise2Sim	39.32±1.42	95.68±0.92	21.92±3.84	97.86±0.47	65.04±5.95	26.18±2.87	36.70±2.33	95.99±0.71	30.36±9.17	97.21±0.71	64.39±7.62	20.68±3.63
AdaReNet	40.80±3.56	96.47±0.32	20.44±13.33	98.43±0.13	72.41±6.04	28.21±3.29	43.47±0.64	97.90±0.55	14.56±2.47	99.14±0.12	76.34±2.79	32.33±1.21
Unsupervised												
IPDM	41.32±0.99	96.78±0.80	17.81±3.61	98.45±0.43	72.90±4.80	28.07±2.28	42.30±0.74	97.84±0.55	15.39±1.36	98.36±0.36	75.30±4.76	30.32±1.30
Self-supervised												
TurnDiff (ours)	42.41±1.21	96.90±0.83	15.30±2.21	98.71±0.33	73.64±5.44	28.25±2.35	42.85±0.77	97.95±0.40	14.46±1.38	98.95±0.23	76.45±3.79	31.54±2.11

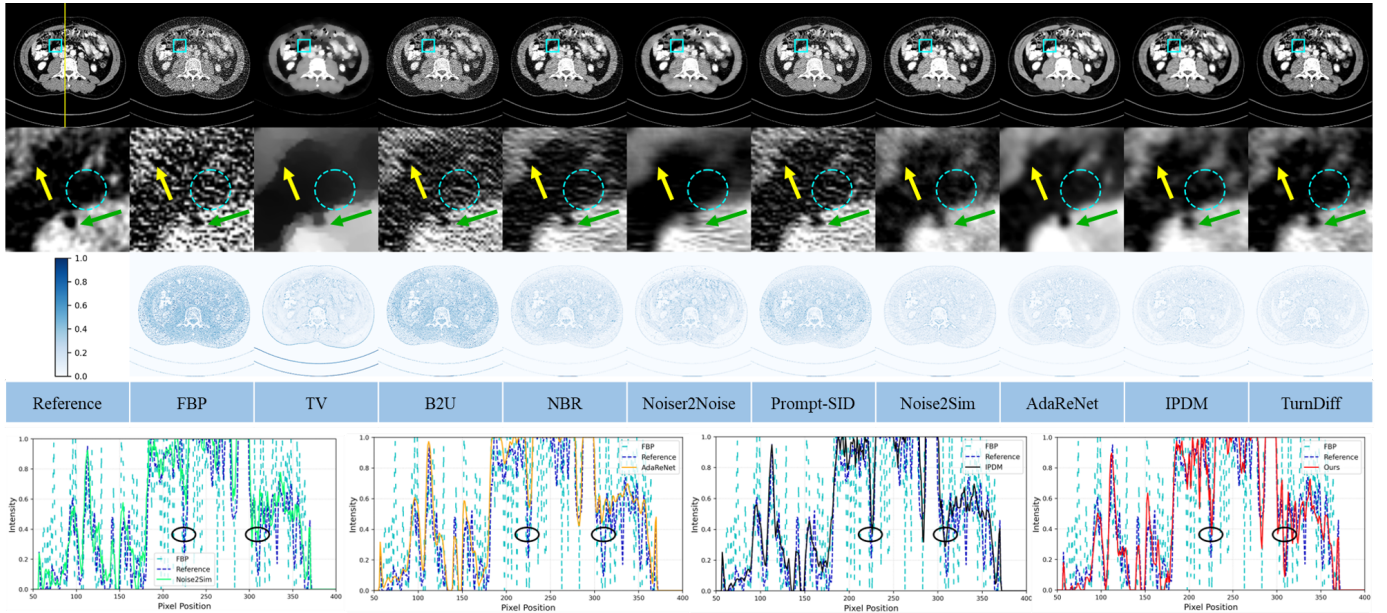


Fig. 6. Qualitative results of a 25% dose CT image from the Mayo dataset. Qualitative assessment against the Mayo 25% dose dataset in the abdomen. The line graphs show the fit of Noise2Sim, AdaReNet, IPDM, which are similar to the models in this study, to the reference in a column, respectively. The display window is [-100,200] HU.

where fan-beam projections y_{ld} and y_0 represent low-dose and full -dose CT data. An incident photon count $I_0 = 1.5 \times 10^5$ and electronic noise variance $\sigma_e^2 = 10$ were used for simulation. The scanning geometry featured a source-to-rotation center distance of 1361.2 mm and detector-to-rotation center distance of 615.18 mm, with 720 views acquired over 360-degree. Images were reconstructed via FBP at 512×512 resolution. Datasets were simulated at 50%, 25%, and 10% dose levels, with 8 cases used for training and 2 cases ($L067, L096$) reserved for testing.

2) *LIDC-IDRI dataset*: To further validate the model, this study utilized the publicly available dataset LIDC-IDRI (Lung Image Database Consortium and Image Database Resource Initiative) [37]. It is a publicly available lung nodule dataset, which is mainly used to study early cancer detection in high-risk populations. The dataset contains a total of 1018 lung CT scan images from 1010 lung patients. After preprocessing, a simulation approach similar to that of the Mayo dataset was taken to derive 25%, 10% dose data. Finally, 45 patients were selected for training and 5 patients for testing.

3) *Real clinical dataset*: The real clinical data contained a total of 500 LDCT image domain images with a pixel resolution of 512×512 and a projection domain of 720×720 . These data were acquired using a GE scanner (Discovery CT750 HD) at 120 kVp, 80 mAs and 1.25 mm slice thickness. In this work, real clinical data were used only for testing to verify the generalizability and validity of this study in real LDCT. To be precise, real data were tested directly using models trained on the LIDC-IDRI dataset.

B. Implementation Details

The contextual sub-data projection domain model adopts a U-Net architecture similar to [38], though with two down-sampling stages removed to accommodate projection domain dimensions. Training employs an Adam optimizer with initial learning rate 0.0003, batch size 8, and 100 epochs, with learning rate halved every 20 epochs. The latent diffusion module utilizes a four-layer autoencoder and a four-layer Transformer-based denoising network. Diffusion training uses AdamW optimizer with initial learning rate 0.0003, cosine annealing

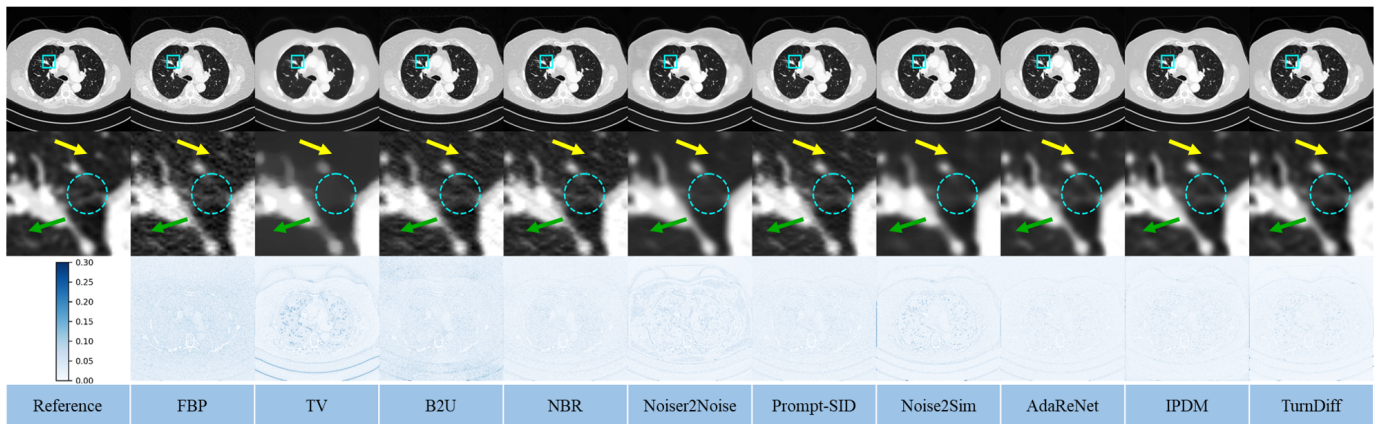


Fig. 7. Qualitative assessment in the lungs against the Mayo 25% dose dataset. The blue region of interest is zoomed in to show the difference, and the green and yellow arrows point to lesions with significant disparity. The display window is $[-1350, 200]$ HU.

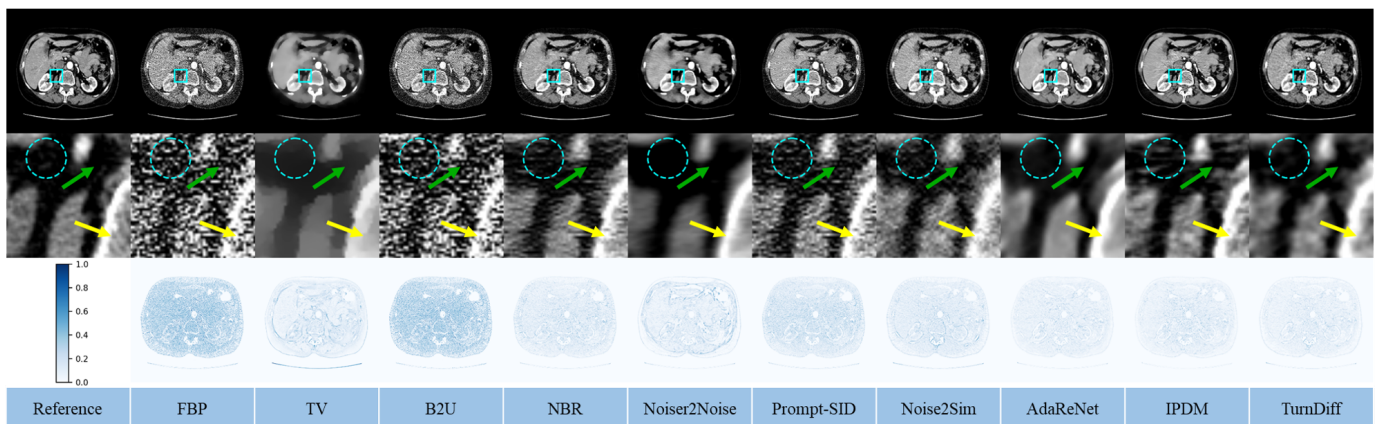


Fig. 8. Qualitative assessment against the LIDC-IDRI 25% dose dataset in the abdomen. The blue region of interest is zoomed in to show the difference, and the green and yellow arrows point to lesions with significant disparity. The display window is $[-100, 200]$.

scheduler, $T = 1000$ diffusion steps, $T_L = 5$ sampling steps, batch size 4, and 60 epochs. All experiments were implemented in PyTorch on an NVIDIA RTX 4090D GPU (24GB), requiring approximately 5 hours for projection domain training and 20 hours for image domain training. Source code is made available at <https://github.com/yqx7150/TurnDiff>.

In order to evaluate the state-of-the-art of this study, we selected traditional denoising methods and several self-supervised/unsupervised methods for comparison. These include Total Variation (TV) [39], B2U [40], Neighbor2Neighbor (NBR) [26], Noiser2Noise [25], Prompt-SID [33], Noise2Sim [15], AdaReNet [41], and IPDM [21].

C. Evaluation Metrics

To validate the clinical feasibility of the method, three other metrics that are close to the radiologist’s judgment of the condition were introduced in this study: feature similarity index (FSIM) [43], visual information fidelity (VIF) [44], and noise quality metric (NQM) [45]. All metrics were calculated under the CT window $[-1024, 3072]$ HU.

D. Experiment Results

1) *Evaluation of different datasets*: This study quantitatively validates the model’s superiority using 25% dose data from

the Mayo and LIDC-IDRI datasets. Comparative experiments against traditional methods, self-supervised approaches, and clean-data-based iterative diffusion methods demonstrate the advancement of our approach from multiple perspectives, as clearly shown in Fig. 6 through full images, zoomed regions, and residual maps. While traditional TV regularization achieves noise removal, it causes over-smoothing and compromises pathological features, with parameter sensitivity across different scanning conditions. Deep learning-based B2U suffers performance degradation due to limited adaptability to structured CT noise. Noiser2Noise introduces excessive randomness by adding artificial noise, leading to texture loss similar to TV methods. Prompt-SID, despite incorporating diffusion models and cue learning, shows limited effectiveness on the Mayo dataset. NBR, lacking our similarity enhancement strategy, produces less distinct lesion visualization in both lung and abdominal scans, as evidenced in Fig. 6 and Fig. 7.

As can be seen from Table I, Noise2Sim, AdaReNet, and IPDM all showed good results, but Noise2Sim’s method based on batch data similarity requires higher data z-axis orientation, which resulted in a significant drop in metrics across different datasets, and the overly randomized selection of similar data can easily lead to drifting of CT values as shown in Figs. 6 and 8. However, our method mitigates the CT value mismatch due

TABLE II

QUANTITATIVE GENERALIZATION RESULTS (MEAN±STD) ON DIFFERENT DOSES LEVEL FROM THE MAYO 2016 DATASET AND THE LIDC-IDRI DATASET. THE BEST RESULTS ARE HIGHLIGHTED IN BOLD.

Methods	Mayo Dataset 25% → 10%			Mayo Dataset 25% → 50%			LIDC-IDRI Dataset 25% → 10%			LIDC-IDRI Dataset → Mayo Dataset 25% → 50%		
	PSNR↑	SSIM(%)↑	RMSE↓	PSNR↑	SSIM(%)↑	RMSE↓	PSNR↑	SSIM(%)↑	RMSE↓	PSNR↑	SSIM(%)↑	RMSE↓
Baseline/Tradition												
FBP	26.60±4.04	49.79±13.28	105.38±58.21	34.98±2.26	81.44±7.24	36.84±9.60	32.20±4.33	70.79±15.97	55.93±30.78	34.98±2.26	81.44±7.24	36.84±9.60
TV	38.21±2.47	94.30±2.49	24.74±9.21	39.41±1.20	85.24±6.20	24.83±2.68	39.05±1.21	80.03±0.34	40.03±3.61	39.41±1.20	85.24±6.20	24.83±2.68
Self-supervised												
B2U	29.94±4.51	68.75±12.36	73.50±43.38	37.36±2.24	89.23±5.01	28.03±7.55	34.56±4.52	81.32±11.77	43.59±28.67	36.93±2.22	88.20±5.35	29.44±7.84
Neighbor2Neighbor	34.13±4.67	82.13±10.58	46.30±30.85	41.13±1.67	95.59±1.83	17.88±3.62	38.31±4.28	91.06±7.06	28.31±20.77	40.62±1.75	94.95±2.24	19.00±4.06
Noiser2Noise	32.11±6.52	77.39±15.33	67.33±59.56	39.68±0.84	95.78±1.15	20.83±2.04	37.03±3.80	92.04±7.17	32.22±23.99	36.70±1.13	95.46±0.96	29.48±3.87
Prompt-SID	31.81±4.36	73.28±11.89	58.94±35.08	39.21±1.92	92.72±3.34	22.44±5.15	36.75±4.43	86.61±9.45	33.83±22.89	39.23±1.93	92.78±3.35	22.41±5.20
Noise2Sim	36.14±4.67	90.99±6.54	37.92±32.10	39.86±1.36	96.31±0.70	20.58±5.56	35.73±3.17	93.91±3.35	35.61±19.40	36.24±2.42	95.51±1.10	32.04±9.05
AdaReNet	33.29±9.36	86.26±13.66	81.95±13.66	42.47±1.12	97.43±0.56	15.17±2.06	40.98±3.91	96.23±4.53	20.31±16.27	42.13±0.64	97.20±0.48	16.99±1.21
Unsupervised												
IPDM	38.02±4.27	91.46±9.27	29.53±22.78	41.93±0.76	97.35±0.52	16.07±1.43	40.59±3.10	95.73±3.83	21.30±11.05	41.57±0.70	97.18±0.61	16.73±1.39
Self-supervised												
TurnDiff (ours)	40.82±1.44	96.13±1.11	18.44±3.30	43.11±1.10	97.46±0.53	14.09±1.85	41.14±4.02	96.26±4.01	20.95±20.06	41.85±0.98	97.40±0.52	16.25±1.89

to the pixel-level weighted correction that achieves a balance in suppressing noise and preserving details. Notably, although the effect on the LIDC data is lower than that of AdaReNet, it requires independent noisy data with the same information, which cannot be strictly classified as self-supervised, and as shown in Fig. 8, the image produces a smoothing of the details on the muscle tissues and bones, which can interfere with the diagnostic performance of the radiologist to a large extent.

Our method best matches the reference in intensity variation, as shown in the line profile in Fig. 6, demonstrating superior reconstruction robustness. Crucially, our approach operates solely on single LDCT projection during both training and inference, offering a truly self-supervised solution suitable for label-scarce clinical environments.

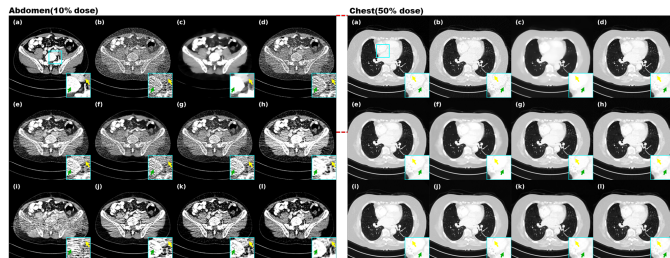


Fig. 9. Display of results on up and down dose generalization for (a) Reference (b) FBP (c) TV (d) B2U (e) NBR (f) Noiser2Noise (g) Prompt-SID (h) Noise2Sim (i) AdaReNet (j) IPDM (k) TurnDiff-Up/Down and (l) TurnDiff (ours). The display window for abdomen images is [-100, 200] HU and for chest images is [-1350, 200] HU.

2) *Experiment results of tunable generalization*: While self-supervised methods typically suffer from degraded generalization when pre-trained models are applied to different dose levels, this study demonstrates the feasibility and superior generalization capability of our approach across varying doses. As shown in Fig. 9 and Table II, our method achieves a breakthrough lead in both quantitative metrics and visual quality for 10% dose abdominal data. Although AdaReNet performs slightly better on lung data, its performance degrades significantly on abdomen data, while our model effectively suppresses scattering artifacts—a capability not possessed by other methods. In addition, the difference between the up and down dose strategies exhibited in Fig. 9 is a good indication of the correctness of the generalization strategy for

adjustability. Inspired by NEED, we also generalize the LIDC-IDRI pre-trained model to the Mayo dataset, confirming its reconstruction capability on unseen data.

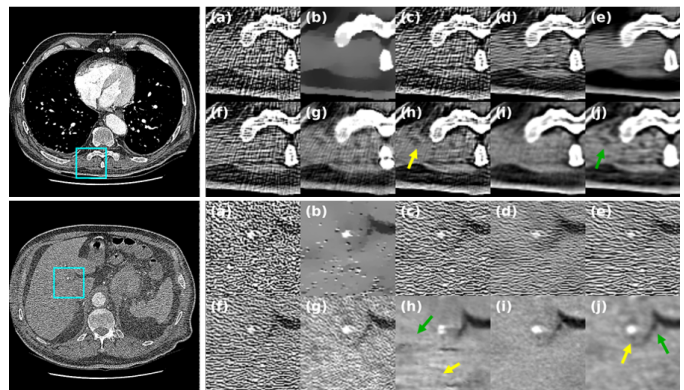


Fig. 10. Generalized results from real clinical data. (a) FBP (b) TV (c) B2U (d) NBR (e) Noiser2Noise (f) Prompt-SID (g) Noise2Sim (h) AdaReNet (i) IPDM (j) TurnDiff (ours). The display window is [-100, 200] HU.

3) *Representation of real clinical data*: Since the data used for training and testing were obtained in a simulated manner, to better validate the clinical usability of the method, we took several cases from real patients for the study. As demonstrated in Fig. 10, our method outperforms AdaReNet in detail recovery and noise suppression. It effectively removes noise around lesions while preserving diagnostic features—capabilities crucial for clinical practice. IPDM exhibits smoothing and detail loss after dual-domain processing, while Noise2Sim obscures structurally important regions. Though other methods surpass FBP, they show limited adaptability to real noise patterns. On the contrary, our TurnDiff removes the noise to a large extent and the pathological features are well reconstructed. It will bring a new paradigm to self-supervised denoising methods.

E. Ablation Study

1) *Validity of the dual domain strategy*: This study first presents a holistic analysis of the proposed framework and performs ablation studies on single projection and overall stages. As shown in Fig. 11 and Table III, denoising solely in the projection domain reveals inadequate noise suppression, incomplete recovery of muscle tissue details, and suboptimal

TABLE III

ABLATION STUDIES (MEAN \pm STD) ON THE PROPOSED MODULES AND λ ON 25% DOSE TEST DATA FROM THE MAYO DATASET.

Proj.	Imag.	PSNR \uparrow	SSIM(%) \uparrow	RMSE \downarrow	Dissimilarity	PSNR \uparrow	SSIM(%) \uparrow	RMSE \downarrow	λ	PSNR \uparrow	SSIM(%) \uparrow	RMSE \downarrow
\checkmark	\times	41.11 \pm 1.07	95.52 \pm 1.03	17.73 \pm 2.28	\checkmark	41.09 \pm 0.87	95.46 \pm 0.62	17.52 \pm 1.79	$\lambda = 0.5$	42.21 \pm 1.09	96.88 \pm 0.66	15.61 \pm 2.03
									$\lambda = 1$	42.28 \pm 1.24	96.79 \pm 0.95	15.54 \pm 2.33
\checkmark	\checkmark	42.41\pm1.21	96.90\pm2.49	15.30\pm2.21	\times	41.11\pm1.07	95.52\pm1.03	17.73\pm2.28	$\lambda(\text{ours})$	42.41\pm1.21	96.90\pm2.49	15.30\pm2.21

restoration of skeletal structures. These limitations are effectively addressed through subsequent knowledge distillation in the image domain, demonstrating that the initial reconstruction \hat{x}_0 and original data x_{ld} serve as complementary guidance, compensating for each other's limitations during the reconstruction process.

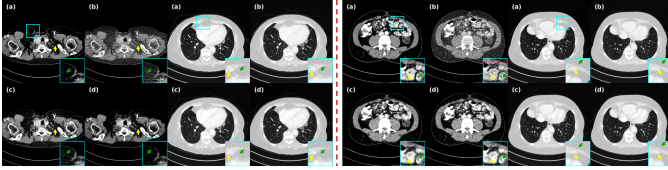


Fig. 11. Ablation studies to verify the effectiveness of two-stage and the importance of similarity enhancement perception. Left: (a) Reference (b) FBP (c) Only projection (d) TurnDiff (**ours**). Right: (a) Reference (b) FBP (c) No enhance (d) TurnDiff (**ours**). The display window for abdomen images is [-100, 200] HU and for chest images is [-1350, 200] HU.

2) *Importance of self-enhancing similarity in projection domain*: After analyzing the effectiveness of the dual-domain phase, we focus on the proposed self-enhancing similarity strategy in the projection domain phase. This strategy is proposed to shorten the dissimilarity between contextual sub-data. So it focuses on highlighting the loss weight of similarity and ignoring the excessive part of dissimilarity. As shown in Fig. 11 and Table III, implementations without this strategy exhibit feature smoothing and gradient disappearance, impairing the subsequent image-domain refinement stage's ability to discriminate between noise and tissue structures, ultimately leading to suboptimal performance.

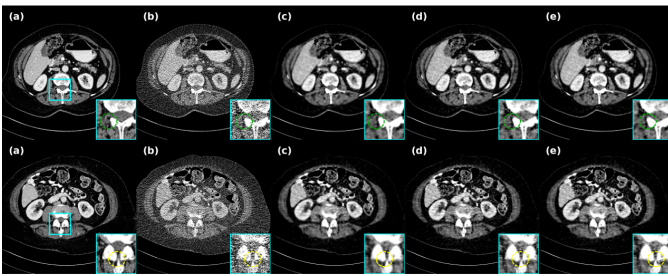


Fig. 12. Ablation studies on the effectiveness of pixel-level weighted fusion. (a) Reference (b) FBP (c) $\lambda = 0.5$ (d) $\lambda = 1$ (e) TurnDiff (**ours**). The display window for abdomen images is [-100, 200] HU.

3) *Pixel-level self-correcting validity and difference from fixed weights*: Subsequently, we carried out the difference between self-correction at the pixel level of the inference process and taking fixed weights. Fig. 12 and Table III add fully illustrate the situation, with fixed weights we selected λ as 0.5, and even selected λ as 1, even though this is not in line with the original intent of the dual-stage. As can be seen, our pixel-level fusion can make a balance between \hat{x}_0 and x_{ld} for each pixel, laying

the groundwork for entering into image inference, and showing competitive results in both metrics and reconstruction.

V. DISCUSSION

This study investigates a solution for LDCT reconstruction that relies solely on single LDCT projection data, requiring neither paired nor clean data. This is a critical challenge in both deep learning and clinical diagnostics. While our method demonstrates promising results, some reconstructed lung and abdominal images still exhibit incomplete recovery of fine vasculature and subtle blurring in localized pathological regions. We attribute this limitation to substantial corruption of such details by noise, which cannot be fully compensated without clean data-driven distribution modeling. Meanwhile, the value of $N_{x_{ld}}^{25\%}$ varies in different scanning instruments. This paper only studies the feasibility of adjustable generalization. Future work will incorporate multi-device physics factors into the reconstruction process, aiming to achieve stronger generalization performance even in the absence of target data.

VI. CONCLUSION

In this study, we proposed a novel self-supervised method, TurnDiff, for low-dose CT denoising, and it was also the first self-supervised LDCT denoising method that combines the diffusion model. The main contributions of TurnDiff were 1) proposed a self-enhancing similarity strategy for contextual sub-data, which mitigated image smoothing and provided the initial a priori as a foundation for the follow-up. 2) Combined the initial a priori with latent diffusion depth in the form of knowledge distillation. 3) The pixel-level self-correcting fusion technique in the inference process enabled the fusion of the initial a priori with the balanced LDCT image, and the technique also provided support for generalizing the contextual sub-data. Both training and testing of TurnDiff only required the LDCT projection domain, making it a truly self-supervised denoising method.

APPENDIX

A. Proof of Eq. (9)

Define $s_1(y_{ld})$, $s_2(y_{ld})$, and $s(y_0)$ as the noisy sub-data, noisy sub-target, and clean sub-data. $\varepsilon_1 = \mathbb{E}_{s_2(y_{ld})|s_1(y_0)}(s_2(y_{ld})) - s(y_0)$, $w(\varepsilon_1) = 1 - \varepsilon_1$. For supervised learning:

$$\begin{aligned} & \mathbb{E}_{y_0, y_{ld}} \| w(\varepsilon_1) \odot (f_\theta(s_1(y_{ld})) - s(y_0)) \|_2^2 \\ &= \mathbb{E} \| w(\varepsilon_1) \odot (f_\theta(s_1(y_{ld})) - s_2(y_{ld}) + s_2(y_{ld}) - s(y_0)) \|_2^2, \end{aligned} \quad (20)$$

under the independent condition that $s(y_0)$ exists, using the vector norm expansion:

$$\begin{aligned} & \mathbb{E}_{y_0, y_{1d}} \| w(\varepsilon_1) \odot (f_\theta(s_1(y_{1d})) - s_2(y_{1d})) \|_2^2 \\ &= \mathbb{E}_{y_0, y_{1d}} \| w(\varepsilon_1) \odot (f_\theta(s_1(y_{1d})) - s(y_0)) \|_2^2 + w(\varepsilon_1)^2 \sigma_{s_2(y_{1d})}^2 \\ & - 2\varepsilon_1 \mathbb{E}_{y_0, y_{1d}} (w(\varepsilon_1)^2 \odot (f_\theta(s_1(y_{1d})) - s(y_0))), \end{aligned} \quad (21)$$

when $\varepsilon_1 \rightarrow 0$, the noise pairs exhibit high similarity, effectively approximating supervised loss performance. However, when similarity regions show substantial variation, Eq. (8) increasingly diverges from supervised error. To mitigate this, we introduce $w(\varepsilon_1)$, which can also eliminate unreliable regions to approximate the supervision loss when $\varepsilon_1 \rightarrow 1$ (the context constraint always has similarity). Together, ε_1 and $w(\varepsilon_1)$ serve as intelligent regulators—thus validating the first term of Eq. (9).

Defining ε_2 as the output sampling discrepancy, we establish that both input discrepancy ε_1 and output discrepancy jointly constrain denoising consistency: small input discrepancy should correspond to small output discrepancy.

REFERENCES

- [1] D. J. Brenner and E. J. Hall, “Computed tomography—an increasing source of radiation exposure,” *N. Engl. J. Med.*, vol. 357, no. 22, pp. 2277–2284, 2007.
- [2] R. Smith-Bindman *et al.*, “Radiation dose associated with common computed tomography examinations and the associated lifetime attributable risk of cancer,” *Arch. Intern. Med.*, vol. 169, no. 22, pp. 2078–2086, 2009.
- [3] A. Sodickson *et al.*, “Recurrent CT, cumulative radiation exposure, and associated radiation-induced cancer risks from CT of adults,” *Radiology*, vol. 251, no. 1, pp. 175–184, 2009.
- [4] M. Balda, J. Hornegger, and B. Heismann, “Ray contribution masks for structure adaptive sinogram filtering,” *IEEE Trans. Med. Imag.*, vol. 31, no. 6, pp. 1228–1239, 2012.
- [5] E. Y. Sidky and X. Pan, “Image reconstruction in circular cone-beam computed tomography by constrained, total-variation minimization,” *Phys. Med. Biol.*, vol. 53, no. 17, p. 4777, 2008.
- [6] Y. Chen *et al.*, “Artifact suppressed dictionary learning for low-dose CT image processing,” *IEEE Trans. Med. Imag.*, vol. 33, no. 12, pp. 2271–2292, 2014.
- [7] A. Manduca *et al.*, “Projection space denoising with bilateral filtering and CT noise modeling for dose reduction in CT,” *Med. Phys.*, vol. 36, no. 11, pp. 4911–4919, 2009.
- [8] J. Wang *et al.*, “Penalized weighted least-squares approach to sinogram noise reduction and image reconstruction for low-dose x-ray computed tomography,” *IEEE Trans. Med. Imag.*, vol. 25, no. 10, pp. 1272–1283, 2006.
- [9] K. Dabov *et al.*, “Image denoising by sparse 3-D transform-domain collaborative filtering,” *IEEE Trans. Image Process.*, vol. 16, no. 8, pp. 2080–2095, 2007.
- [10] H. Shan *et al.*, “Competitive performance of a modularized deep neural network compared to commercial algorithms for low-dose CT image reconstruction,” *Nat. Mach. Intell.*, vol. 1, no. 6, pp. 269–276, 2019.
- [11] G. Wang *et al.*, “Deep learning for tomographic image reconstruction,” *Nat. Mach. Intell.*, vol. 2, no. 12, pp. 737–748, 2020.
- [12] J. Shen *et al.*, “Mlf-iosc: multi-level fusion network with independent operation search cell for low-dose CT denoising,” *IEEE Trans. Med. Imag.*, vol. 42, no. 4, pp. 1145–1158, 2022.
- [13] H. Chen *et al.*, “Low-dose CT with a residual encoder-decoder convolutional neural network,” *IEEE Trans. Med. Imag.*, vol. 36, no. 12, pp. 2524–2535, 2017.
- [14] J. Lehtinen *et al.*, “Noise2Noise: Learning image restoration without clean data,” *arXiv preprint arXiv:1803.04189*, 2018.
- [15] C. Niu *et al.*, “Noise suppression with similarity-based self-supervised deep learning,” *IEEE Trans. Med. Imag.*, vol. 42, no. 6, pp. 1590–1602, 2022.
- [16] T. Garber and T. Tiran, “Image restoration by denoising diffusion models with iteratively preconditioned guidance,” in *Proc. IEEE/CVF Conf. Comput. Vis. Pattern Recognit.*, 2024, pp. 25,245–25,254.
- [17] J. Ho, A. J. Jain, and P. Abbeel, “Denoising diffusion probabilistic models,” *Adv. Neural Inf. Process. Syst.*, vol. 33, pp. 6840–6851, 2020.
- [18] Y. Song *et al.*, “Score-based generative modeling through stochastic differential equations,” *arXiv preprint arXiv:2011.13456*, 2020.
- [19] E. Hogeboom, J. Heek, and T. Salimans, “simple diffusion: End-to-end diffusion for high resolution images,” in *Int. Conf. Mach. Learn.*. PMLR, 2023, pp. 13,213–13,232.
- [20] K. Zheng *et al.*, “Dpm-solver-v3: Improved diffusion ode solver with empirical model statistics,” *Adv. Neural Inf. Process. Syst.*, vol. 36, pp. 55,502–55,542, 2023.
- [21] F. Liao *et al.*, “Domain progressive low-dose CT Imaging using Iterative Partial Diffusion Model,” *IEEE Trans. Med. Imaging*, 2024.
- [22] H. Nam *et al.*, “Contrastive denoising score for text-guided latent diffusion image editing,” in *Proc. IEEE/CVF Conf. Comput. Vis. Pattern Recognit.*, 2024, pp. 9192–9201.
- [23] V. T. Hu *et al.*, “Self-guided diffusion models,” in *Proc. IEEE/CVF Conf. Comput. Vis. Pattern Recognit.*, 2023, pp. 18,413–18,422.
- [24] J. Batson and L. Royer, “Noise2self: Blind denoising by self-supervision,” in *Int. Conf. Mach. Learn.*. PMLR, 2019, pp. 524–533.
- [25] N. Moran *et al.*, “Noisier2noise: Learning to denoise from unpaired noisy data,” in *Proc. IEEE/CVF Conf. Comput. Vis. Pattern Recognit.*, 2020, pp. 12,064–12,072.
- [26] T. Huang *et al.*, “Neighbor2neighbor: A self-supervised framework for deep image denoising,” *IEEE Trans. Image Process.*, vol. 31, pp. 4023–4038, 2022.
- [27] Y. Wang *et al.*, “SVB: Self-Supervised Real CT Denoising via Similarity-Based Visual Blind-Spot Scheme,” *IEEE Trans. Instrum. Meas.*, 2024.
- [28] Q. Wu *et al.*, “Unsharp structure guided filtering for self-supervised low-dose CT imaging,” *IEEE Trans. Med. Imag.*, vol. 42, no. 11, pp. 3283–3294, 2023.
- [29] M. O. Unal, M. Ertas, and I. Yildirim, “Proj2Proj: self-supervised low-dose CT reconstruction,” *PeerJ Comput. Sci.*, vol. 10, p. e1849, 2024.
- [30] Q. Gao *et al.*, “Corediff: Contextual error-modulated generalized diffusion model for low-dose CT denoising and generalization,” *IEEE Trans. Med. Imag.*, vol. 43, no. 2, pp. 745–759, 2023.
- [31] Q. Gao *et al.*, “Noise-Inspired Diffusion Model for Generalizable low-dose CT Reconstruction,” *arXiv preprint arXiv:2506.22012*, 2025.
- [32] B. Yang *et al.*, “LFDT-Fusion: A latent feature-guided diffusion Transformer model for general image fusion,” *Inf. Fusion*, vol. 113, p. 102639, 2025.
- [33] H. Li *et al.*, “Prompt-SID: Learning Structural Representation Prompt via Latent Diffusion for Single Image Denoising,” in *Proc. AAAI Conf. Artif. Intell.*, vol. 39, no. 5, 2025, pp. 4734–4742.
- [34] M. Zhussip, S. Soltanayev, and S. Y. Chun, “Extending stein’s unbiased risk estimator to train deep denoisers with correlated pairs of noisy images,” *Adv. Neural Inf. Process. Syst.*, vol. 32, 2019.
- [35] T. R. Moen *et al.*, “Low-dose CT image and projection dataset,” *Med. Phys.*, vol. 48, no. 2, pp. 902–911, 2021.
- [36] D. Zeng *et al.*, “A simple low-dose x-ray CT simulation from high-dose scan,” *IEEE Trans. Nucl. Sci.*, vol. 62, no. 5, pp. 2226–2233, 2025.
- [37] S. G. Armato III *et al.*, “The lung image database consortium (LIDC) and image database resource initiative (IDRI): a completed reference database of lung nodules on CT scans,” *Med. Phys.*, vol. 38, no. 2, pp. 915–931, 2011.
- [38] S. Laine *et al.*, “High-quality self-supervised deep image denoising,” *Adv. Neural Inf. Process. Syst.*, vol. 32, 2019.
- [39] L. I. Rudin, S. Osher, and E. Fatemi, “Nonlinear total variation based noise removal algorithms,” *Physica D*, vol. 60, no. 1–4, pp. 259–268, 1992.
- [40] Z. Wang *et al.*, “Blind2unblind: Self-supervised image denoising with visible blind spots,” in *Proc. IEEE/CVF Conf. Comput. Vis. Pattern Recognit.*, 2022, pp. 2027–2036.
- [41] H. Liu *et al.*, “Rotation-Equivariant Self-Supervised Method in Image Denoising,” in *Proc. IEEE/CVF Conf. Comput. Vis. Pattern Recognit.*, 2025, pp. 12,720–12,730.
- [42] Z. Wang *et al.*, “Image quality assessment: from error visibility to structural similarity,” *IEEE Trans. Image Process.*, vol. 13, no. 4, pp. 600–612, 2004.
- [43] L. Zhang *et al.*, “FSIM: A feature similarity index for image quality assessment,” *IEEE Trans. Image Process.*, vol. 20, no. 8, pp. 2378–2386, 2011.
- [44] H. R. Sheikh and A. C. Bovik, “Image information and visual quality,” *IEEE Trans. Image Process.*, vol. 15, no. 2, pp. 430–444, 2006.
- [45] N. Damera-Venkata *et al.*, “Image quality assessment based on a degradation model,” *IEEE Trans. Image Process.*, vol. 9, no. 4, pp. 636–650, 2000.